ROYAL SOCIETY
OF CHEMISTRY

PAPER

Check for updates

(NH₄)₂HPO₄-mediated closed-pore/pseudographite synergy in thin-walled hard carbon for enhanced Na⁺ storage and kinetics

Yatao Chang,†[a] Zhengpeng Yang,†[a] Yufang Cao,†*[b] Zhao He,[cd] Huili Fu,[b] Tongtong Qin,[b] Liming Zhao*[b] and Yongyi Zhang ⓘ *[bc]

Synchronously designing pseudo-graphitic domains featuring expanded interlayer spacing, rich closed pores and short ion transfer paths is crucial to enhancing sodium-ion (Na⁺) kinetics and storage of hard carbon anodes for fast-charging sodium-ion batteries (SIBs), yet remains challenging due to their inherent trade-off. Herein, we propose a (NH₄)₂HPO₄ (DAP)-assisted oxidative etching strategy to tailor kapok-derived carbon precursors with abundant nanopores and crosslinked functional groups, thus stimulating the development of closed pores and graphitic domains during carbonization. The resulting N/P-doped thin-walled (∼600 nm) hard carbon features extended graphitic domains coupled with expanded interlayer spacings and rich closed pores. The unique thin-walled structure can effectively shorten the ion diffusion pathway in-plane and along the thin-walled skeleton. More importantly, expanded graphitic domains with N/P co-doping and rich closed pores can not only provide sufficient active sites for Na⁺ storage through surface adsorption, intercalation, and pore-filling mechanisms but also rapidly construct Na⁺ diffusion channels during intercalation. Consequently, the as-prepared hard carbon anode exhibits superior capacity and remarkable rate performance (334.5 mAh g⁻¹/0.1C and 196.4 mAh g⁻¹/20C) without sacrificing the initial coulombic efficiency (ICE) (92.1%).

1. Introduction

Sodium-ion battery (SIB) has emerged as a highly promising option for large-scale energy storage applications due to the abundant sodium resource and fast-charging capability.[1–4] However, the practical deployment of SIBs is hindered by the sluggish kinetics of Na⁺ insertion/extraction, primarily due to the large ionic radius of Na⁺, which impose stringent requirements on anode materials.[5,6] Among carbonaceous candidates, biomass-derived hard carbons stand out for their tunable microstructures, including pseudo-graphitic domains, defects, and pores,[7–9] which enable multi-mechanism sodium storage (adsorption, intercalation, and pore filling).[10,11] Despite these merits, conventional hard carbons suffer from unsatisfactory plateau capacity (<0.1 V *vs.* Na⁺/Na), sluggish ion kinetics, and

insufficient active sites, particularly under high-rate conditions.[12–14]

A critical challenge lies in reconciling the inherent trade-off between closed-pore engineering and graphitization. Closed pores, embedded within randomly stacked graphitic domains, are essential for enhancing low-voltage plateau capacity by accommodating Na⁺ *via* pore-filling mechanisms.[15–17] However, their formation typically requires high carbonization temperatures (>1500 °C), which inevitably reduce interlayer spacing (<0.38 nm) and impede Na⁺ intercalation kinetics.[18,19] Conversely, lower carbonization temperatures (≤1200 °C) yield larger interlayer spacings (>0.40 nm) but result in excessive defects and sparse closed pores, compromising reversible capacity and ICE.[20] Pre-oxidation methods (*i.e.*, air/acid treatment) partially address this dilemma by inducing closed pores at lower temperatures, yet they simultaneously hinder graphitization through rigid crosslinked structures (*e.g.*, C–O–C groups).[21,22] This structural paradox underscores the need for innovative strategies to synchronize pore-graphitic synergy. Moreover, the presence of closed pores can sieve out the solvated Na⁺ to limit the electrolyte decomposition, thereby contributing to high ICE values of hard carbon anodes.[16] Beyond nanoscale optimization, the macroscopic architecture of hard carbons plays an equally pivotal role. Conventional micron-sized granular carbons exhibit tortuous ion pathways and limited interfacial contact, whereas two-dimensional (2D)

aSchool of Materials Science and Engineering, Henan Polytechnic University, Jiaozuo 454003, China

bKey Laboratory of Multifunctional Nanomaterials and Smart Systems, Suzhou Institute of Nano-Tech and Nano-Bionics, Chinese Academy of Sciences, Suzhou 215123, China. E-mail: yfcao2019@sinano.ac.cn; lmzhao2019@sinano.ac.cn; yyzhang2011@sinano.ac.cn

cDivision of Nanomaterials and Jiangxi Key Lab of Carbonene Materials, Jiangxi Institute of Nanotechnology, Nanchang 330200, China

dCollege of Chemistry and Chemical Engineering, Nanchang University, 999 Xuefu Avenue, Nanchang 330031, China

† These authors contributed equally to this work.

This journal is © The Royal Society of Chemistry 2025

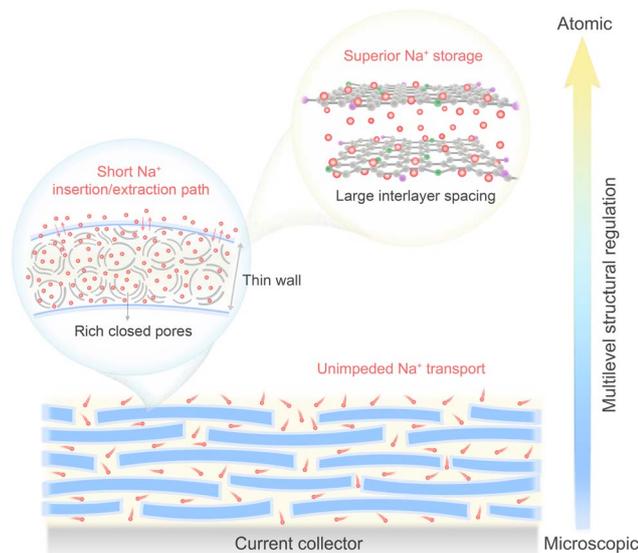*J. Mater. Chem. A*, 2025, **13**, 36677–36688 | **36677**

Fig. 1 Schematic diagram showing the structural feature of the kapok-derived DAP-HC anode.

thin-walled structures inherently shorten in-plane and through-thickness ion diffusion distances.[23,24] Natural kapok fibers, with their intrinsic hollow and thin-walled morphology (~600 nm wall thickness), provide an ideal precursor for constructing such hierarchical architecture.[25]

Capitalizing on this unique geometry, we proposed a DAP-assisted oxidative etching strategy to engineer N/P-doped thin-walled hard carbons with synergistic features of abundant closed pores, extended graphitic domains, and expanded interlayer spacing (Fig. 1). The induction of open nanopores, crosslinked functional groups and partial carbonization during DAP-assisted pre-oxidation can effectively promote the formation of closed pores and graphitic domains during carbonization, overcoming the traditional temperature-dependent trade-off. Such integrated thin-walled architecture can provide sufficient active sites for Na$^+$ storage and fast Na$^+$ transport pathways, including short diffusion paths in-plane and along the thin-walled skeleton as well as fast Na$^+$ intercalation channels in extended graphitic domains coupled with expanded interlayer spacings and rich closed pores. The optimized anode exhibits a superior sodium storage capacity (334.5 mAh g^{-1} at 0.1C), remarkable rate performance (196.4 mAh g^{-1} at 20C), and a high ICE (92.1%), showing a great application potential for fast-charging SIBs.

2. Experimental section

2.1. Preparation of hard carbon materials derived from kapok fiber

The kapok-derived hard carbon materials were prepared by the pre-treatment, pre-oxidation, and high-temperature carbonization. Initially, the kapok fiber was immersed in anhydrous ethanol for 6 h at 50 °C, and then washed several times with deionized water to remove lipid impurities and ash content

from the fiber surface. The resultant cleared kapok fiber (CKF) was dried overnight in a vacuum oven at 60 °C. For the pre-treatment, 10 g of DAP was dissolved in deionized water and mixed with the dried kapok fiber (10 g). This mixture was dried in an oven at 100 °C, with stirring every hour to ensure that DAP fully penetrated the internal structure of CKF. The CKF was then heated to 220 °C in a tube furnace at a rate of 5 °C min^{-1} for 2 h under an air atmosphere. Subsequently, the pre-oxidized sample was stirred with 2 M HCl for 2 h at 80 °C to remove any remaining impurities. The resulting precursor was washed with deionized water until neutral, then subjected to ultrasonic treatment for 6 h, and drying overnight at 80 °C. The as-obtained DAP-assisted pre-oxidation kapok fiber (DAP-OKF) was transferred to a tube furnace and pyrolyzed at 1200 °C for 2 h under an argon atmosphere, with a heating rate of 5 °C min^{-1}, to produce N/P-doped hard carbon materials. Finally, the material underwent an additional pickling step, followed by washing with distilled water until pH = 7. After being dried at 80 °C for 24 h, the final product, DAP-mediated hard carbon, is denoted as DAP-HC. For comparison, the CKF was processed under the same conditions without the addition of DAP, and the resulting hard carbon material is designated as OHC. PHC was prepared under the same conditions with DAP replaced by phosphoric acid. Additionally, DHC was prepared by directly carbonizing the CKF at 1200 °C.

2.2. Characterization

The surface morphologies of samples were obtained using field emission scanning electron microscopy (SEM) (THERMO SCIENTIFIC, Apreo C HiVac, America) and high-resolution transmission electron microscopy (HRTEM) (Talos F200S). The thermogravimetric analysis (TGA) was carried out using a TG209F1 NETZSCH instrument in the temperature range of 30–1000 °C at a heating rate of 10 °C min^{-1} under a N$_2$ atmosphere with a flow rate of 20 mL min^{-1}. The structures of the obtained samples were investigated by XRD (Bruker D8) with the Cu Ka radiation, set at the operating voltage of 40 kV (k = 0.154 nm). Raman spectra were obtained using a laser Raman spectrometer (Alpha300R, WITec GmbH, Germany) with a wavelength of 532 nm as the excitation source. The coin-type half cells of DAP-HC electrodes were assembled through a customized battery mold device. The *in situ* confocal micro-Raman spectrometer (LabRAM HR Evolution) was used to conduct the *in situ* Raman testing on the electrodes prepared. The current density of the cells was set at 30 mA g^{-1} (with a voltage range of 0.01–2.5 V). The chemical components were characterized by X-ray photoelectron spectroscopy (XPS) (Thermo Scientific Nexsa), and pore characterization of kapok-based carbon materials was performed by the Brunauer–Emmett–Teller (BET) (ASAP 2020, China) method and small-angle X-ray scattering (SAXS) (Xeuss 2.0, Xenocs, France). To analyze the SAXS data, the Porod equation was used:[26]

$$I(Q) = \frac{A}{Q^a} + \frac{Ba_1{}^4}{\left(1 + a_1{}^2 Q^2\right)^2} + D \tag{1}$$

36678 | *J. Mater. Chem. A*, 2025, **13**, 36677–36688

This journal is © The Royal Society of Chemistry 2025

where A and B are proportional to the total surface areas of the large and small pores, respectively. Q is the scattering vector and D is a constant background term. The diameters of closed nanopores can be obtained from the a_1 value ($R = 2a_1 10^{1/2}$).

2.3. Electrochemical measurements

The galvanostatic charge and discharge, cycle, rate and galvanostatic intermittent titration technique (GITT) testing were performed on the LAND CT2001A instruments (Wuhan, China). Cyclic voltammetry (CV) and electrochemical impedance spectra (EIS) measurements were performed on a CHI660D electrochemical workstation (Chenhua, Shanghai). All electrochemical measurements were carried out at room temperature in the potential range of 0.01–2.5 V (relative to Na$^+$/Na).

To understand the kinetics of Na$^+$ storage in hard carbons, GITT was carried out with a 30 mA g^{-1} of pulse current for 20 min between the rest intervals for 2 h. The diffusion D_{Na^+} is calculated using the following generalized formula, based on Fick's second law:[27]

$$D_{Na^+} = \frac{4}{\pi\tau}\left(\frac{m_b V_m}{M_b S}\right)^2\left(\frac{\Delta E_s}{\Delta E_t}\right)^2 \quad (2)$$

where τ is the pulse duration, m_b is the mass of the active material, V_m is the molar volume of the electrode material, S is the surface area of active material, ΔE_s is the voltage change caused by the pulse, and ΔE_t is the voltage change of the galvanostatic charge/discharge process. ΔE_s and ΔE_t can be obtained from GITT curves.

According to Trasatti and Dunn's method, the electrochemical reaction kinetics of all anodes was investigated based on CV curves at different scan rates (0.2–10 mV s^{-1}). The measured peak specific current density (i) and scan rate (v) conform to the following equations:[28]

$$\log(i) = b \times \log(v) + \log(a) \quad (3)$$

$$i = av^b \quad (4)$$

here a and b are reaction-related constants. It is well known that if the parameter $b = 0.5$, the electrochemical reaction is a diffusion-controlled process, whereas, if the parameter $b = 1$, it will be a capacitive-controlled process. The b values can be estimated from the slope curve plotted between $\log(v)$ and $\log(i)$.

The surface capacitive contribution (k_1v) and diffusion-limited faradaic contribution ($k_2v^{1/2}$) can be further quantified according to the following equation:[28]

$$i(V) = k_1v + k_2v^{1/2} \quad (5)$$

where v represents the scan rate, $i(V)$ is the current response at the specific potential, and both k_1 and k_2 are constants.

Voltage maintenance was achieved by first charging the battery to 2.5 V, followed by 50 days resting period.

The anodes were prepared using kapok fiber derived hard carbons, super P, carboxy methyl cellulose (CMC), and styrene–butadiene latex binder (SBR) in a mass ratio of 91 : 1.5 : 2.5 : 5. After the mixture was stirred for 60 min, the slurry was scraped on the copper foil, and put in a vacuum drying oven at 100 °C for 12 h. Subsequently, the resulting anode was cut into discs with about 12 mm in diameter. Sodium foil was used as a counter electrode and Whatman GF/A glass fibers as a separator. The coin cell (CR2032) was assembled in an argon-filled glovebox using 1 M NaPF$_6$ in diethylene glycol dimethyl ether as an electrolyte. The copper foil with a radius of 12 mm is loaded with about 1.5–2.5 mg of electrode materials.

3. Results and discussion

DAP-HC was synthesized *via* a two-step process involving acid pre-oxidation and carbonization, as illustrated in Fig. 2a. Initially, the hollow-structured CKF was pre-oxidized with DAP, followed by ultrasonic crushing to yield thin-walled tile-shaped DAP-OKF. During pre-oxidization at low temperatures, (NH$_4$)$_2$HPO$_4$ can promote catalytic dehydration and oxidative cyclization of CKF,[29] facilitating the formation of open nanopores, N/P-containing functional groups and partial carbonized structure. These structural modifications are critical for templating closed pores and pseudo-graphitic domains during subsequent carbonization. The thin-walled DAP-OKF was then pyrolyzed at 1200 °C under argon protection to obtain the final DAP-HC, characterized by extended graphitic domains coupled with expanded interlayer spacings and rich closed pores. In contrast, control samples (DHC and OHC) obtained from the carbonization of CKF and air-oxidized CKF (OKF) exhibit minimal closed pores and smaller interlayer spacings, highlighting the indispensable role of DAP in pore-graphitic synergy.

SEM reveals that CKF exhibits a thin-walled hollow microtube morphology (Fig. 2b and S1). After DAP-assisted pre-oxidation and ultrasonic crushing treatment, the DAP-OKF shows a quasi-2D tile shape with an approximate lateral size of 5 μm (Fig. 2c and S2), well inheriting the natural thin-walled (~600 nm) structure of CKF. By contrast, OKF without DAP-assisted etching still maintains the natural hollow morphology of natural CKF (Fig. S3), which is very difficult to break into fragments due to the preservation of the intrinsic organic structure. Moreover, a distinct chromatic transition from the milky-white CKF to black DAP-OKF (Fig. S4) suggests partial carbonization during the DAP-mediated oxidative etching process. This structural evolution can be proved by the carbon lattice distortions within DAP-OKF *via* HRTEM (Fig. 2d). The high density of quantum dot-like features suggests rich open nanopores (~1 nm in diameter) induced into DAP-OKF.[24] These open pores can act as nucleation sites for closed-pore formation during subsequent carbonization.[30]

The detailed pore structures of DAP-OKF are evaluated by N$_2$ adsorption–desorption. Consistent with the HRTEM results, the DAP-OKF exhibits typical type I isotherms with abundant nanopores (~1 nm), contrasting sharply with the mesopore-dominated (~4 nm) structures of OKF and CKF (Fig. 3a and S5). The specific surface area (SSA) of DAP-OKF (45.79 m^2 g^{-1}) significantly exceeds that of OKF (10.98 m^2 g^{-1}) and CKF (9.59 m^2 g^{-1}) (Table S1), confirming the effectiveness of DAP etching in generating microporous structures. These open pores serve as templates for the subsequent formation of closed pores
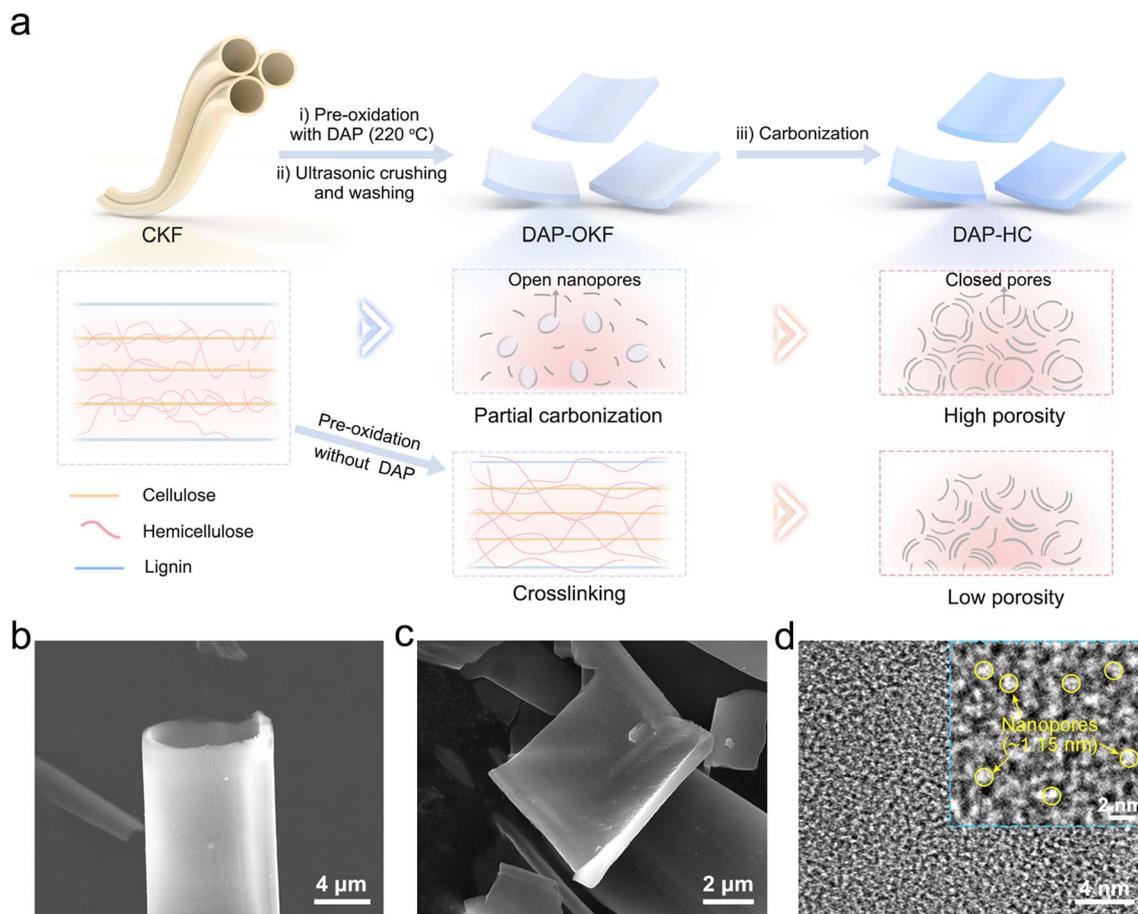
This journal is © The Royal Society of Chemistry 2025

J. Mater. Chem. A, 2025, **13**, 36677–36688 | **36679**

Fig. 2 Fabrication of DAP–HC and its precursor micromorphology. (a) Schematic illustration of the preparation procedure. (b) SEM image of CKF. SEM (c) and HRTEM (d) images of DAP–OKF.

during high-temperature carbonization.[31] Notably, when phosphoric acid was used as an alternative etchant under the same conditions, the resulting precursor (denoted as P-OKF) exhibits a granular morphology with thin-walled structure collapse (Fig. S6) and an excessively high SSA of 561.25 m^2 g^{-1}, indicating severe over-etching and the formation of abundant open pores (Fig. S7).[32] This difference in etching behavior of DAP with pure H_3PO_4 can be attributed to the following reason: DAP can decompose to generate NH_3 and H_3PO_4 during oxidation. The released NH_3 creates a mildly reducing atmosphere that moderates the aggressive oxidative etching of H_3PO_4, resulting in controlled and suitable pore development without destroying the thin-walled structure.[29] Therefore, for hollow structured CKF with high cellulose content, DAP is more suitable as an activator than H_3PO_4.

X-ray diffraction (XRD) was performed to realize the crystal structure of DAP–OKF. As shown in Fig. 3b, CKF and OKF display crystalline cellulose peaks at 15.3°, 22°, and 33.4°, while DAP–OKF exhibits a broad (002) peak at 23.24°,[33,34] characteristic of turbostratic carbon, confirming partial carbonization during oxidative etching. This phenomenon facilitates the formation of graphite-like structures during high-temperature carbonization, which can be validated by TEM characterization of the final product. Fig. 3c shows the TGA of different

precursors. DAP–OKF exhibits higher carbon yield (34.7 wt%) than CKF and OKF, with no discernible decomposition peak in the derivative thermogravimetry (DTG) curve (Fig. S8). This result demonstrates that DAP-assisted pre-oxidation not only fundamentally alters the pyrolytic decomposition pathways of CKF, but also facilitates a more efficient conversion of cellulose to high-yield char (partial carbonization and crosslinked structures) as the precursor material for hard carbon.[29] In contrast, OKF and CKF show rapid weight loss at 200–400 °C from cellulose/lignin decomposition, yielding lower carbon residues (19.0 wt% and 9.5 wt%, respectively).

XPS reveals the surface chemical evolution of precursors during DAP-mediated oxidative etching. Compared to pristine CKF, both DAP–OKF and OKF exhibit decreased carbon content and increased oxygen content, attributed to dehydration and oxidation reactions induced by O_2 or/and DAP (Fig. S9a). Strikingly, DAP–OKF shows significant nitrogen doping (6.41 at%) and trace phosphorus incorporation (0.43 at%) (Table S2), confirming the successful introduction of N/P-functional groups during DAP-assisted pre-oxidation. Specifically, C 1s spectra (Fig. 3d) can be deconvoluted into peaks at 284.2, 285.0, 286.4, 287.8 and 289.0 eV, representing sp^2-C, sp^3-C, C–O, C=O and C–O–C=O bonds, respectively. Compared with OKF and CKF, the increase of sp^2-C and C–O–C=O in DAP–OKF indicates

36680 | J. Mater. Chem. A, 2025, 13, 36677–36688
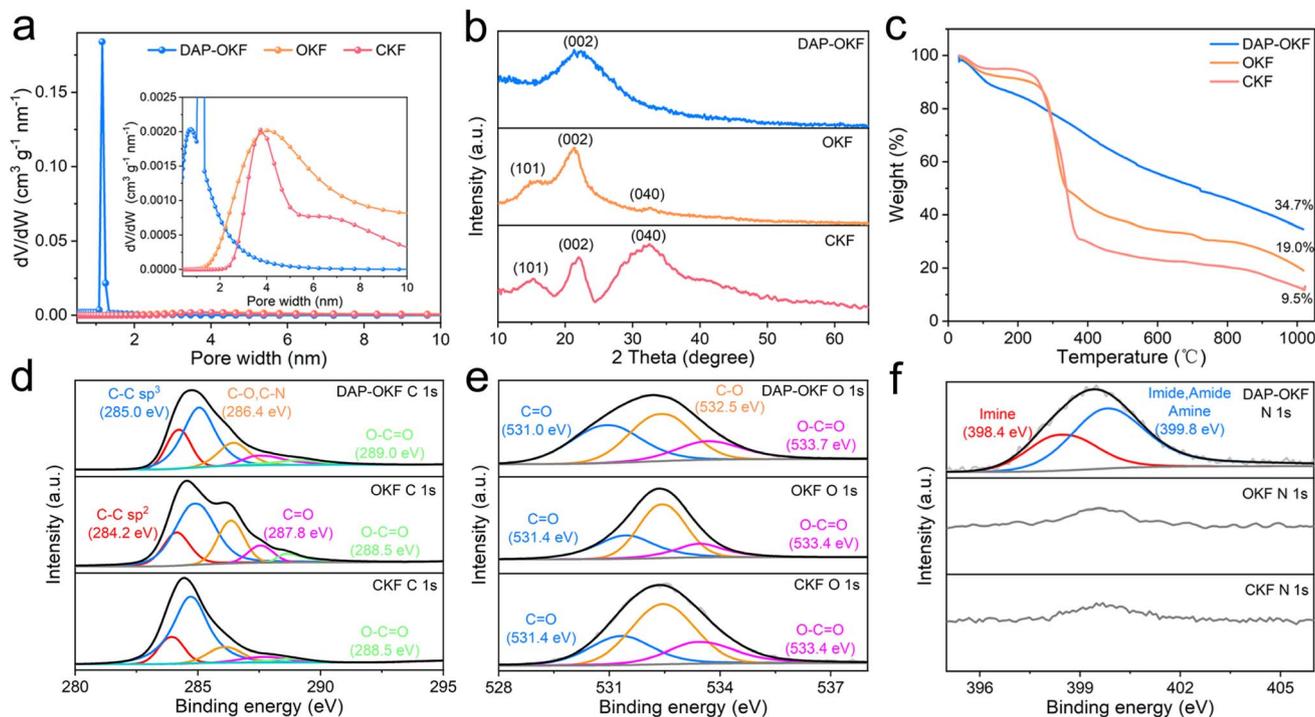
This journal is © The Royal Society of Chemistry 2025

Fig. 3 Structure and pyrolysis behavior characterization of DAP-OKF, OKF and CKF precursors. (a) Pore-size distribution curves. (b) XRD patterns. (c) TGA curves. (d–f) High-resolution XPS spectra.

that DAP-etching can promote both dehydration and cyclization of CKF, forming a highly stable aromatized carbon framework. This structure can serve as an ideal precursor for subsequent high-temperature graphitization, promoting the growth of graphitic microdomains.[35] Moreover, the presence of C–O–C= O (anhydride or ester group) groups can facilitate the development of the pseudo-graphite structure with larger carbon interlayer spacing and closed pores during carbonization.[36] Consistent with C 1s results, DAP-OKF exhibits dominant C=O and C–O–C=O contributions, contrasting with CKF's predominant C–O (Fig. 3e). These oxygenated moieties can stabilize the carbon framework.

Fig. 3f shows the high-resolution spectrum of N 1s in DAP-OKF. The N 1s spectra can be deconvoluted into two peaks at 398.4 eV and 399.8 eV corresponding to –C=N–C– (imine) and –C–N– (imide, amide, amine), respectively. These nitrogen-containing groups on the one hand can facilitate the formation of the crosslinked structure and on the other hand can be converted into the high-activity pyridinic-N/pyrrolic-N, improving the ion-adsorption kinetics. Moreover, the deconvolution of the P 2p spectrum can help identify three characteristic peaks at 132.3 eV (C–P–O$_3$), 133.8 eV (P–O–C), and 135.4 eV (–PO$_4$). These P-containing groups further confirm the esterification reaction between H$_3$PO$_4$ decomposed by DAP and CKF during pre-oxidation (Fig. S9b).[29] Note that such trace amounts of C–O–P and C–P–O$_3$ can not only effectively mitigate structural deformation caused by carbon layer shrinkage during high-temperature treatments, but also can induce charge redistribution, enhancing interlayer electron cloud repulsion and expanding interlayer spaces.[32,37]

HRTEM images show the effects of different precursor pretreatment methods on the microstructure of carbon microcrystals. DHC without pretreatment exhibits a highly disordered carbon matrix (Fig. 4a), while OHC shows an even more disordered turbostratic structure and few closed pores (Fig. 4b). Such difference is mainly attributed to the inhibition of graphitization because of excessive C–O–C=O crosslinks formed during direct oxidation. In contrast, DAP-HC displays more interconnected pseudo-graphitic nanodomains interspersed with abundant closed pores and expanded interlayer spacing (0.408 nm) (Fig. 4c). Such superior pseudo-graphitic domains are associated with the formation of a highly stable aromatized carbon framework, N/P-containing groups and nanopores in precursors during DAP-assisted pre-oxidation treatment. The formed closed pores and expanded interlayer spacing can reduce the energy barrier for Na$^+$ insertion between carbon layers, facilitating enhanced Na$^+$ diffusion kinetics.[38]

The detailed crystallographic differences can be quantified via XRD, as shown in Fig. 4d. All samples of DAP-HC, OHC and DHC exhibit two broad peaks at around 23° and 43.5°, corresponding to the lattice planes of (002) and (100), respectively. The obvious shift of the (002) peak to a smaller angle is observed for DAP-HC in comparison with OHC (0.387 nm) and DHC (0.380 nm), suggesting its increased interlayer spacing (0.402 nm), which is consistent with HRTEM results. The expanded interlayer spacing can be directly attributed to introduction of nanopores and N,P-doping during DAP-assisted oxidative etching, which can reduce the intercalation barrier of Na$^+$ and improve the intercalation capacity.[39] Moreover, the larger lateral crystallite size ($L_a = 4.85$ nm) and thicker crystallites ($L_c = 1.49$

This journal is © The Royal Society of Chemistry 2025

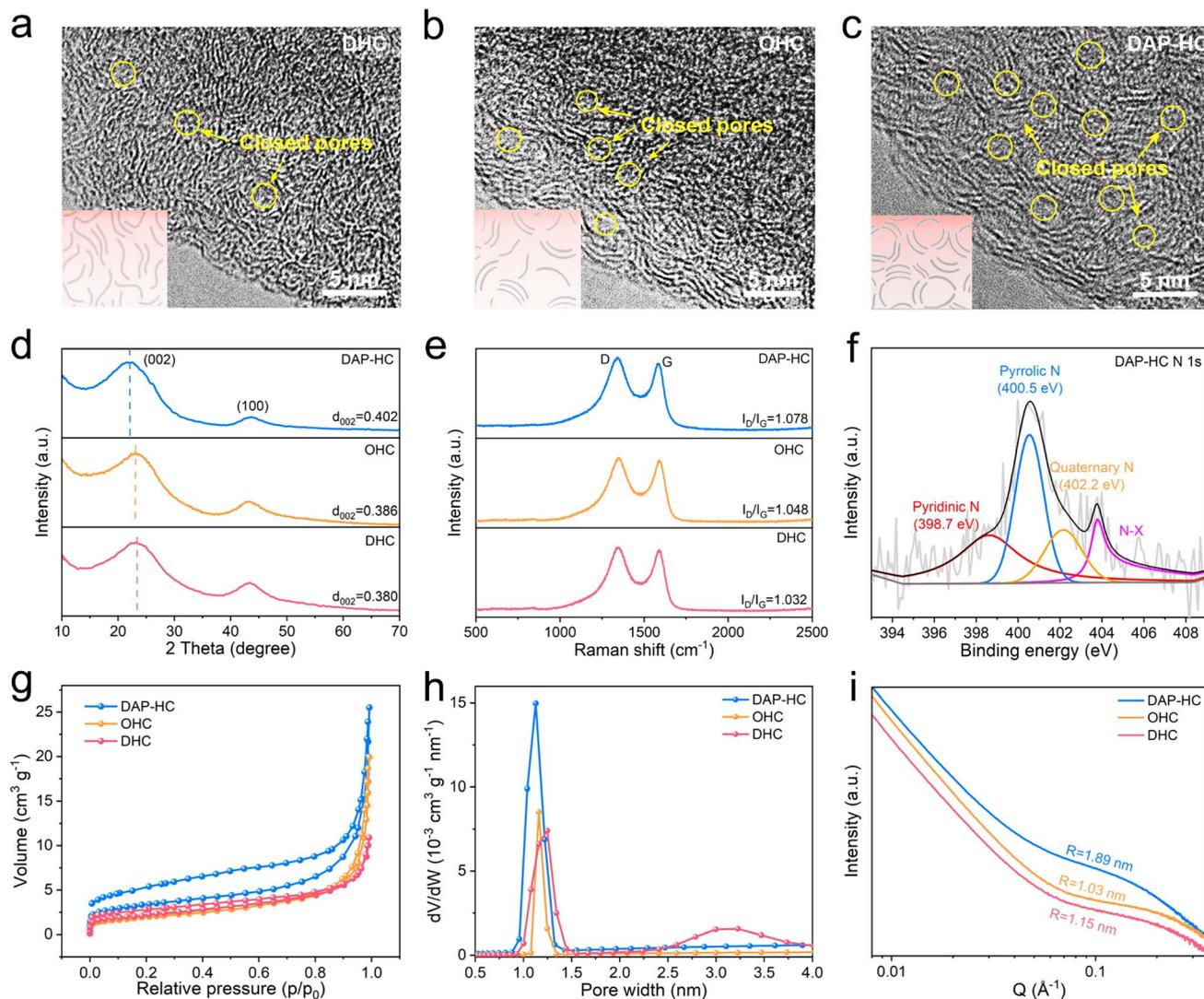J. Mater. Chem. A, 2025, 13, 36677–36688 | 36681

Fig. 4 Structural characterization of DHC, OHC and DAP-HC. (a–c) HRTEM images. (d) XRD patterns. (e) Raman spectra. (f) High-resolution N 1s spectra of DAP-HC. (g and h) N$_2$ adsorption–desorption isothermal curves and pore size distributions. (i) SAXS patterns.

nm) of DAP-HC (Table 1) further confirm the generation of more graphitic domains during high-temperature carbonization, which might be stimulated by the stable aromatized carbon framework formed in DAP-OKF during pre-oxidation.

Raman spectra were further investigated to evaluate the microcrystalline structure of carbon materials (Fig. 4e). All samples of DAP-HC, OHC and DHC exhibit two characteristic peaks around 1350 and 1580 cm^{-1}, corresponding to disordered carbon (D band) and sp^2 graphitized carbon (G band),

respectively.[39] The narrowed G band of DAP-HC suggests an increased domain size of the graphitic microcrystals in a 2D plane, which is consistent with XRD results. Such a relatively long-range graphitic layer is crucial for fast charge transfer kinetics at the interface. Furthermore, the increased I_D/I_G (1.078) of DAP-HC compared to OHC (1.048) and DHC (1.05) provides direct evidence of elevated defect density. These increased defects are closely related to high porosity and heteroatom-doping within the carbon matrix of DAP-HC.

Table 1 Structural parameters estimated from XRD, Raman, SAXS and N$_2$ adsorption–desorption results

Sample	XRD			Raman	SAXS	N$_2$ adsorption	
	d_{002} (nm)	L_c (nm)	L_a (nm)	I_D/I_G	R (nm)	S_{BET} (m^2 g^{-1})	V_{pore} (cm^3 g^{-1})
DAP-HC	0.402	1.494	4.850	1.078	1.890	12.640	0.038
OHC	0.387	1.411	4.457	1.048	1.030	7.830	0.030
DHC	0.380	1.100	4.170	1.032	1.150	7.420	0.016

36682 | J. Mater. Chem. A, 2025, 13, 36677–36688

This journal is © The Royal Society of Chemistry 2025

The successful co-doping and homogeneous distribution of N, P elements within the carbon skeleton were unequivocally confirmed by XPS survey and mapping spectra (Fig. S10 and S11). According to the XPS survey, the N and P contents are 1.91 at% and 0.28 at%, respectively. Deconvolution of the N 1s spectrum (Fig. 4f) reveals four species: pyridinic-N (398.7 eV), pyrrolic-N (400.5 eV), quaternary-N (graphitic-N, 402.2 eV), and pyridine-N-oxide (403.7 eV).[40,41] The electron-rich pyridinic-N and pyrrolic-N serve as highly active sites for Na$^+$ adsorption, effectively weakening the adsorption energy barrier for Na$^+$. In particular, pyridinic-N can not only optimize the Na$^+$ adsorption energy but also accelerate the desorption of Na$^+$, improving the ICE of the final hard carbon.[42,43] The graphitic-N can enhance the electronic conductivity of the entire carbon matrix, thereby drastically accelerating the charge transfer efficiency. Concurrently, the high-resolution P 2p spectrum (Fig. S12) confirms the presence of P–C bonds (*e.g.*, C–P–C at 132.0–134.0 eV), which is an indication of P atoms being incorporated into the carbon framework. The introduction of larger P atoms induces local structural expansion and strain, which not only contributes to the defect density but also aids in enlarging the interlayer spacing,[44] as corroborated by XRD and Raman. Such trace C–P–C groups (0.28 at%) formed in the DAP-HC carbon matrix during the carbonization process can alter the electron cloud distribution of carbon atoms, thus boosting Na$^+$ adsorption and its diffusion kinetics.[44]

The pore structure of DAP-HC, OHC and DHC can be evaluated using N$_2$ adsorption/desorption isotherms and SAXS. As shown in Fig. 4g, both the SSA and pore size of DAP-HC, OHC and DHC are reduced compared to the corresponding precursor, indicating that high-temperature treatment can induce pore shrinkage or closure within the carbon matrix. Notably, DAP-HC demonstrates the highest SSAs of 12.64 m^2 g^{-1}, substantially surpassing those of OHC (7.83 m^2 g^{-1}) and DHC (7.42 m^2 g^{-1}) (Table 1). This distinction underscores the pivotal role of DAP-assisted oxidative etching in modulating pore evolution during carbonization. Note that the hard carbon of PHC still exhibits SSAs after high-temperature treatment, suggesting numerous defects in the carbon matrix (Fig. S13), which is detrimental to its improvement of ICE. Detailed pore size distribution analysis (Fig. 4h) reveals that DAP-HC features a relatively well-developed microporous structure with a dominant pore size distribution from 0.8 to 1.5 nm. Such enhanced SSA and microporosity facilitate rapid Na$^+$ adsorption and transport.

To better characterize the closed pores in the carbon matrix, SAXS was conducted. The pronounced "hump" scattering profile of DAP-HC (Fig. 4i) signifies a substantial formation of closed pores, contrasting with the limited closed porosity in OHC and DHC. The enriched closed pores in DAP-HC can be attributed to the induction of open nanopores and crosslinked functional groups during the DAP-assisted pre-oxidation process, which facilitates Na$^+$ storage in the plateau region. Furthermore, the radius of closed pores was determined using the Porod equation (eqn (2)) based on SAXS curves (Fig. S14 and Table S3). The enlarged radius of closed pores in DAP-HC can

reduce ionic diffusion barriers,[45] thereby enabling fast Na$^+$ kinetics and its efficient storage.

The electrochemical performances of hard carbons were tested in sodium half-cells in the range of 0.01–2.5 V. The first CV curves of DAP-HC, OHC and DHC are shown in Fig. 5a. All curves show a pair of sharp redox peaks at ∼0.10 V/0.02 V and irreversible cathodic peaks at about 0.3–0.8 V, corresponding to the Na$^+$ intercalation within the graphitic layers and the formation of a solid–electrolyte interface (SEI), respectively. DAP-HC shows a much smaller cathodic peak at about 0.60 V compared to OHC and DHC, indicating reduced electrolyte consumption for SEI, which is attributed to the abundant closed-pore structure within the DAP-HC matrix. Besides, the sharpest intensity of the reversible redox peak at 0.1 V in DAP-HC suggests its highest reversible Na$^+$ plateau capacity. Fig. 5b illustrates the initial GCD curves of DAP-HC, OHC and DHC at 0.1C. Influenced by the pseudo-graphitic domains and closed pore structures, all curves present two regions: a sloping region (>0.1 V) corresponding to surface adsorption and intercalation into the carbon layer and a plateau region (<0.1 V) corresponding to the intercalation of Na$^+$ filling into the closed pores.[46,47] Note that the lowest initial discharge voltage (0.98 V) in DAP-HC suggests a significantly small transmission interfacial resistance for ions and electrons, which is closely related to the high surface activity due to its N-doping and rich micropores.[48] Moreover, the DAP-HC demonstrates superior reversible capacity (334.5 mAh g^{-1}) and ICE (92.1%), outperforming OHC (312.7 mAh g^{-1} and 90.88%) and DHC (292.1 mAh g^{-1} and 88.2%). All of DAP-HC, OHC and DHC show a much higher ICE than PHC (84.95%) (Fig. S15). The seriously impeded ICE of PHC indicates that the aggressive etching by phosphoric acid introduces excessive defects and open pores and thereby severely compromising reversibility. The in-depth capacity analysis from the slope- and plateau-voltage regions of all the samples is presented in Fig. 5c. In comparison, the DAP-HC shows both a higher plateau capacity (206.9 mAh g^{-1}) and slope capacity (128.33 mAh g^{-1}) than OHC (196.70 mAh g^{-1}/ 116.85 mAh g^{-1}) and DHC (188.0 mAh g^{-1}/103.40 mAh g^{-1}). Such improved capacity of DAP-HC could be attributed to the optimized graphitic structure coupled with high closed porosity, expanded carbon layer spacing and rational N-doping.

Moreover, both rate and cycling tests were conducted for DAP-HC, DHC and OHC. The charging capacities of DAP-HC are higher than that of OHC and DHC at all rates, and achieves highly reversible charge capacities of 334.5 and 196.4 mAh g^{-1} at 0.1C and 20C (Fig. S16), respectively, highlighting its great ability to maintain capacity even at high rates. In contrast, the control samples of OHC and DHC only deliver the capacity of 173.75 and 108.7 mAh g^{-1} at 20C, respectively, suggesting their poor rate capability (Fig. 5d). Such rate capability of DAP-HC outperforms the state-of-the-art anode materials reported in the literature (Fig. 5e). The plateau and slope capacities at different current densities for different HCs are summarized in Fig. S17. Remarkably, DAP-HC shows a minimum decay in both slope and plateau capacity, suggesting its superior Na$^+$ migration and sodiation kinetics. In comparison, DHC and OHC demonstrate a rapid decay in plateau capacity, thus leading to
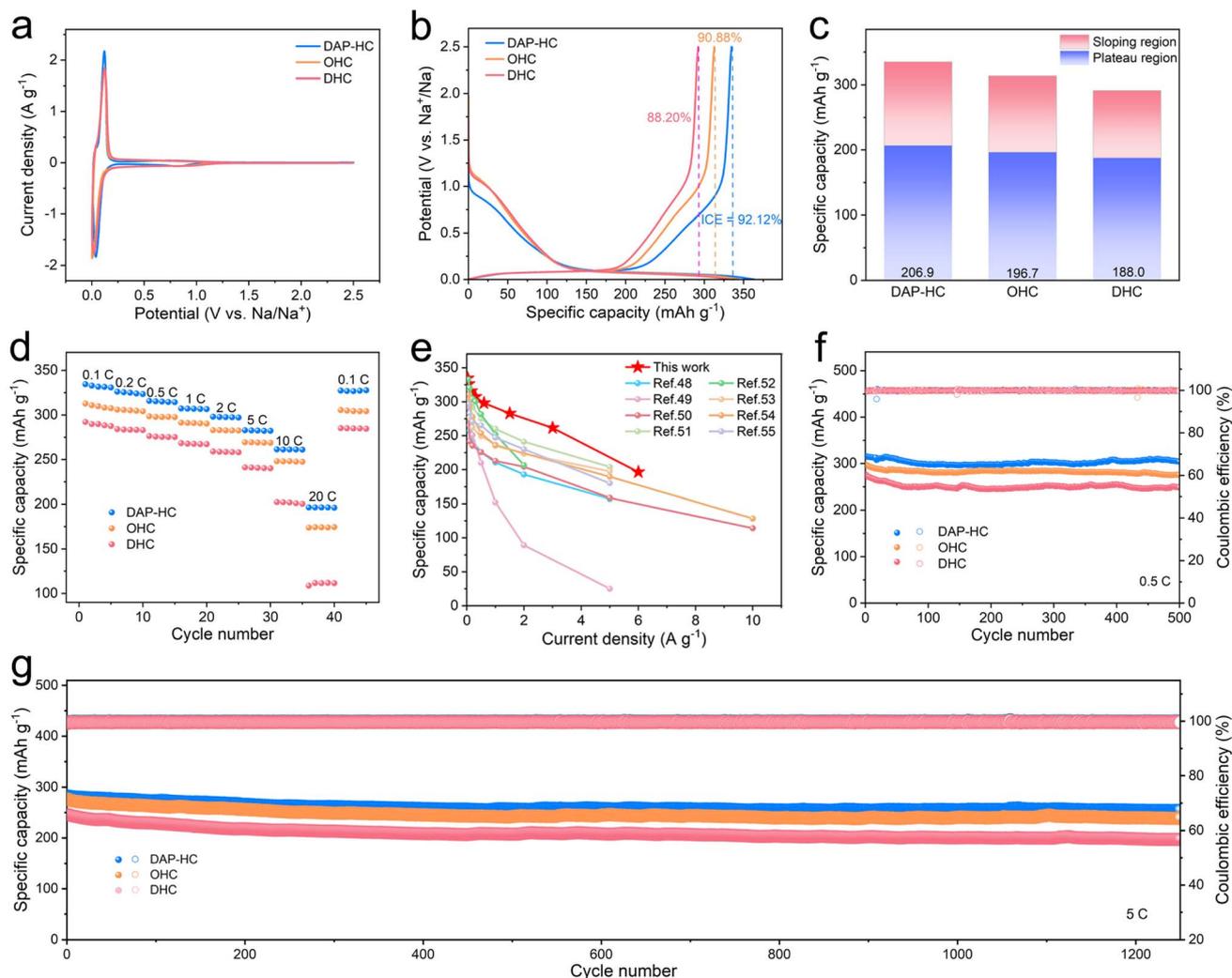
This journal is © The Royal Society of Chemistry 2025

J. Mater. Chem. A, 2025, **13**, 36677–36688 | **36683**

Fig. 5 Electrochemical performance of DAP-HC, OHC and DHC anodes for SIBs. (a) CV curves of the first cycle at 0.2 mV s^{-1}. (b) Initial GCD curves at 0.1C. (c) Specific capacity derived from the plateau region (<0.1 V) and slope region (>0.1 V), based on the second discharge curve. (d) Rate performance at various current rates. (e) Comparison of rate performance between DAP-HC and reported hard carbon anodes. (f and g) Cycling stability.[48–55]

the sharp decrease in the total capacity. This comparison strongly suggests that the loss of slope capacity is the main factor responsible for the poor rate performance in biomass-derived hard carbons. For DAP-HC, the enhanced sodium storage and kinetics can be attributed to its optimized structures: (1) multilevel ion conductive highways, including rapid in-plane ion transport, short Na$^+$ (de)intercalation paths into the thin-walled carbon matrix and favorable interlayer channels; (2) high-speed closed-pores for enhanced high-plateau capacity and sodiation kinetics; (3) effective N-doping for favorable interfacial kinetic behavior. The DAP-HC electrode demonstrates an outstanding cycling stability with ultrahigh capacity retention of 96.38% (303.9 mAh g^{-1}) after 450 cycles at 0.5C (Fig. 5f) and 89.88% (254.2 mAh g^{-1}) after 1250 cycles at 5C (Fig. 5g), significantly superior to the control sample of OHC and DHC, suggesting its excellent long-term stability. The stability of the Na-ion battery based on DAP-HC can also be evaluated by open-circuit voltage holding (Fig. S18). Initially,

a rapid voltage drop is observed, which can be attributed to the structural relaxation and redistribution of sodium ions within the carbon matrix. After this initial adjustment, the voltage remains highly stable with no noticeable decay after 50 days under open-circuit conditions, showing a very low self-discharge rate and exceptional electrochemical stability of the DAP-HC material.

To understand the Na$^+$ storage behavior of DAP-HC, CV curves at various scan rates were further investigated. Compared with OHC and DHC (Fig. S19), DAP-HC exhibits a negligible irreversible reduction peak and almost well-overlapping at the initial curve (Fig. 6a), suggesting less electrolyte consumption for SEI formation and irreversible reactions. Moreover, the shapes of CV curves are well retained with increasing scan rates, demonstrating its small polarization and high-rate performance (Fig. 6b, S20a and d). To further elucidate the Na-storage mechanism, the b values of peaks in the DAP-HC anode were calculated using eqn (3) and (4) based on
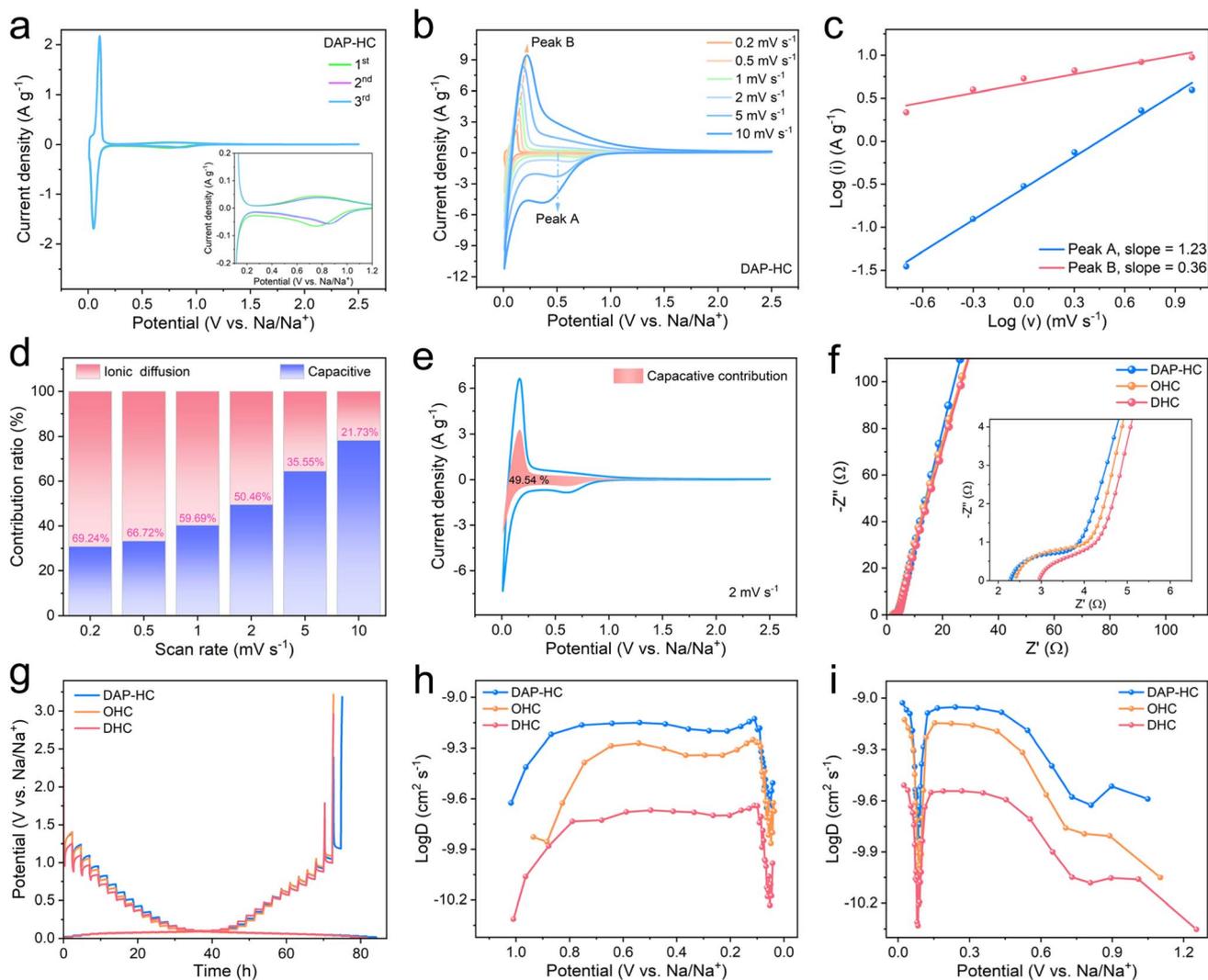
36684 | J. Mater. Chem. A, 2025, 13, 36677–36688

This journal is © The Royal Society of Chemistry 2025

Fig. 6 Kinetic analysis. (a) First three CV cycles of the DAP-HC anode at 0.2 mV s^{-1}. (b) CV curves of the DAP-HC anode at various scan rates and the corresponding correlations between the peak current (*i*) and scan rate (*v*) at peak A and peak B (c). (d) Capacitive contribution percentage of the DAP-HC anode at various scanning rates. (e) CV curve with a calculated capacitive contribution at 2 mV s^{-1}. Nyquist plots (f), GITT potential profiles (g) and Na$^+$ diffusion coefficients in the desodiation (h) and sodiation (i) process of DAP-HC, OHC and DHC anodes.

the CV curves at different scan rates (Fig. 6c). The *b*-values for peak A and peak B in DAP-HC are 1.23 and 0.36, respectively, higher than that of OHC (1.03/0.33) and DHC (0.98/0.3) anodes (Fig. S20b and e). Such results suggest improved Na$^+$ adsorption and intercalation kinetics in DAP-HC, thus leading to a higher contribution rate. To quantify the capacitive (slope capacity) and diffusion-controlled (plateau capacity) contributions of the DAP-HC anode, the CV curves of the DAP-HC anode were further analyzed using eqn (5). Accordingly, the DAP-HC anode shows a higher diffusion contribution of 69.24% at 0.2 mV s^{-1} (Fig. 6d), compared to OHC (66.59%) and DHC (61.67%) (Fig. S20c and f), which might be attributed to its greater Na$^+$ intercalation in extended graphitic domains. As the scan rate increases, the diffusion-controlled contribution decreases while the surface-controlled contribution increases. The relatively high diffusion contribution (50.46%) in the DAP-HC anode (Fig. 6e and S21) at a high scan rate of 2 mV s^{-1} indicates that

more Na$^+$ intercalation into the carbon layer can happen at high rates, suggesting fast Na$^+$ kinetics, thus ensuring fast-charging without severely sacrificing capacity.

Such rapid Na-storage kinetics can also be proved by EIS. As shown in Fig. 6f, the Nyquist plot consists of a semicircle in the high frequency region, Warburg region in the medium frequency region and a straight line in the low frequency region. The depressed semicircle in the high-frequency region is primarily associated with the SEI layer resistance (R_{SEI}) and charge transfer resistance (R_{ct}), which is closely related to the SEI formation and interfacial ionic/electronic conductivity of the hard carbon skeleton. Compared to OHC and DHC, the DAP-HC reveals lower R_{SEI} and R_{ct}. Such decreased impedance of DAP-HC may be ascribed to the combined effects of N-doping, more graphitic structure and rich closed pores for superior electronic/ionic conductivity and improved pre-desolvation.[49]

The Warburg region in the medium frequency and a straight line in the low frequency represent the mass transfer and Na^+ diffusion resistance (Z_w), respectively. Due to the short in-plane ion transfer and ion intercalation paths along the thin-walled carbon matrix, all of DAP-HC, OHC and DHC exhibit a short Warburg region, demonstrating fast ion/mass transfer. Differently, the DAP-HC shows the lowest Z_W value, further demonstrating that the DAP-assisted pre-oxidation treatment for the kapok precursor enables the engineering of the pseudo-graphitic, porous and surface chemical structure in the final hard carbon matrix for fast Na^+ transfer.

To further explore the kinetics, the GITT experiments of DAP-HC, OHC and DHC were conducted using a pulse current of 0.1C for 20 min with rest intervals of 2 h (Fig. 6g). The diffusion coefficients (D_{Na^+}) of different anodes were also calculated based on GITT potential profiles (Fig. 6h and i). It can be found that the D_{Na^+} value varies slightly in the slope region, and a high diffusivity of Na^+ corresponds to the adsorption on the carbon surface. In the plateau region, D_{Na^+} drops sharply with a U-turn feature. The sharp drop of D_{Na^+} around 0.1 V in the plateau region can be ascribed to the slow diffusion kinetics of Na^+ inserted into the graphite-like layer, while the rebound of D_{Na^+} at 0.05 V can be ascribed to a typical pore filling process. In addition, the variation of the D_{Na^+} in the desodiation process is almost opposite to the sodiation process, showing an excellent reversible electrochemical performance. Compared with OHC and DHC, DAP-HC shows a higher D_{Na^+} in the slope regions, suggesting its fastest ion adsorption kinetics. In addition, at around 0.1 V of the sodiation process, the D_{Na^+} of DAP-HC (1.42×10^{-10} cm^2 s^{-1}) is significantly higher than that of OHC (8.4×10^{-11} cm^2 s^{-1}) and DHC (4.7×10^{-11} cm^2 s^{-1}), showing improved Na^+ sodiation kinetics. Such improved kinetics in DAP-HC can be attributed to the multilevel Na^+ diffusion highways, including rapid in-plane transfer, short ion paths in the thin-walled carbon skeleton and favorable migration channels in the expanded carbon interlayer, highlighting its potential for fast charging SIBs.

The structural evolution of the DAP-HC electrode during charge/discharge was further investigated by *in situ* Raman spectroscopy. As shown in Fig. S22, the D and G bands gradually weaken between 2.5 and 0.1 V, while their positions remain largely unchanged, indicating Na^+ adsorption in this stage. Upon further discharging to 0.1–0.05 V, the D band continues to weaken, and the G band shifts to lower frequencies, demonstrating Na^+ intercalation into the carbon layers and the formation of Na–C compounds.[36] When discharged to 0.05–0.01 V, the D band nearly vanishes, suggesting that defects are predominantly covered by Na clusters, consistent with a pore-filling mechanism. Additionally, the presence of quasi-metallic sodium was confirmed by a phenolphthalein colorimetric test using ethanol solution. As illustrated in Fig. S23, a significantly intensified color appears at the fully sodiated state (0.01 V), verifying the substantial presence of metallic sodium.[36]

To further elucidate the effects of N/P doping and closed pores on Na^+ transport and storage performance, density functional theory (DFT) calculations were carried out (see the SI). As illustrated in Fig. S24, several models were constructed, including a pristine bilayer graphene (AB stacking), an N/P co-doped graphitic bilayer, and a closed-pore model composed of three curved graphitic layers. The introduction of N and P heteroatoms into the graphene lattice results in more favorable Na^+ binding energies compared to ideal graphene. Specifically, the N/P co-doped graphitic layer exhibits a higher Na^+ adsorption energy (-1.988 eV) than its pristine counterpart (-0.470 eV), indicating enhanced ionic interaction. Furthermore, the closed-pore model surrounded by N/P-doped graphitic layers shows an even greater binding energy (-2.221 eV), suggesting that closed pores significantly facilitate the thermodynamic feasibility of Na^+ intercalation.

The Na^+ diffusion barrier energies were also evaluated to probe ion mobility within the N/P-doped graphitic domains and closed pores (see the SI). As shown in Fig. S25, the energy profile along the diffusion path (labeled 0–5) was calculated for each model. The results reveal that the diffusion barrier between parallel N/P-doped graphitic layers (0.166 eV) is markedly lower than that in the undoped system (0.459 eV), implying that sodium ions are more readily stored and inserted within the doped interlayers, thereby enhancing the rate capability of DAP-HC. Moreover, the closed-pore model exhibits the lowest diffusion barrier (0.136 eV), underscoring its superior kinetics for Na^+ diffusion. Therefore, in addition to expanded interlayer spacing and N/P co-doping, the presence of closed pores also plays a critical role in promoting the remarkable Na-ion storage performance of DAP-HC.

4. Conclusions

In summary, a DAP-mediated oxidative etching strategy was proposed to resolve the trade-off between closed-pore engineering and graphitization in hard carbons. The N-doped thin-walled carbon ($\sim$600 nm) derived from kapok fibers integrates expanded interlayer spacing (0.402 nm), abundant closed pores, and pseudo-graphitic domains, enabling multilevel Na^+ diffusion highway: (1) rapid in-plane Na^+ diffusion; (2) shortened migration paths along the ultrathin carbon skeleton ($\sim$600 nm); (3) favorable interlayer channels. As expected, the final anode delivers a remarkable rate performance (334.5 mAh g^{-1} at 0.1C and 196.4 mAh g^{-1} at 20C), superior ICE (92.1%) and stable cycling performance. This work provides a novel closed-pore/pseudographite synergy strategy for fast-charging SIB anodes.

Author contributions

Yatao Chang: investigation, writing – original draft, data curation. Zhengpeng Yang: methodology, writing – original draft. Yufang Cao: investigation, writing – review & editing. Zhao He: methodology, formal analysis. Huili Fu: methodology, formal analysis. Tongtong Qin: formal analysis. Liming Zhao: data curation, writing – review & editing. Yongyi Zhang: funding acquisition, writing – review & editing, supervision.

Conflicts of interest

The authors declare that they have no known competing financial interests or personal relationships that could have appeared to influence the work reported in this paper.

36686 | *J. Mater. Chem. A*, 2025, **13**, 36677–36688

This journal is © The Royal Society of Chemistry 2025

Data availability

The data supporting this article have been included as part of the supplementary information (SI). Supplementary information is available. See DOI: **https://doi.org/10.1039/d5ta02820e**.

Acknowledgements

References

1 N. Sun, J. S. Qiu and B. Xu, *Adv. Energy Mater.*, 2022, **12**, 2200715.

2 D. Q. Chen, W. Zhang, K. Y. Luo, Y. Song, Y. J. Zhong, Y. X. Liu, G. K. Wang, B. H. Zhong, Z. G. Wu and X. D. Guo, *Energy Environ. Sci.*, 2021, **14**, 2244–2262.

3 K. F. Wang, F. Sun, Y. L. Su, Y. Q. Chen, J. H. Gao, H. P. Yang and G. B. Zhao, *J. Mater. Chem. A*, 2021, **9**, 23607–23618.

4 H. J. Liang, H. H. Liu, J. Z. Guo, X. X. Zhao, Z. Y. Gu, J. L. Yang, X. Y. Zhang, Z. M. Liu, W. L. Li and X. L. Wu, *Energy Storage Mater.*, 2024, **66**, 103230.

5 Z. Tang, S. Y. Zhou, Y. C. Huang, H. Wang, R. Zhang, Q. Wang, D. Sun, Y. G. Tang and H. Y. Wang, *Electrochem. Energy Rev.*, 2023, **6**, 8.

6 J. H. Zhou and S. J. Guo, *SmartMat*, 2021, **2**, 176–201.

7 K. Schutjajew, P. Giusto, E. Härk and M. Oschatz, *Carbon*, 2021, **185**, 697–708.

8 Z. X. Pei, Q. Q. Meng, L. Wei, J. Fan, Y. Chen and C. Y. Zhi, *Energy Storage Mater.*, 2020, **28**, 55–63.

9 Y. W. Zhou, J. Chen, X. Zhang, J. Y. Peng, L. H. Xue and W. X. Zhang, *Energy Technol.*, 2024, **12**, 2301597.

10 X. Y. Chen, J. Y. Tian, P. Li, Y. Fang, Y. L. Fang, X. M. Liang, J. W. Feng, J. Dong, X. P. Ai, H. X. Yang and Y. L. Cao, *Adv. Energy Mater.*, 2022, **12**, 2200886.

11 X. Han, S. H. Zhou, H. Liu, H. T. Leng, S. Li, J. X. Qiu and F. W. Huo, *Small Methods*, 2023, **7**, 2201508.

12 Y. Chu, J. Zhang, Y. B. Zhang, Q. Li, Y. R. Jia, X. M. Dong, J. Xiao, Y. Tao and Q. H. Yang, *Adv. Mater.*, 2023, **35**, 2212186.

13 Z. Q. Song, M. X. Di, X. Y. Zhang, Z. Y. Wang, S. H. Chen, Q. Y. Zhang and Y. Bai, *Adv. Energy Mater.*, 2024, **14**, 2401763.

14 Y. Liu, J. Yin, R. Y. Wu, H. Zhang, R. Zhang, R. Q. Huo, J. X. Zhao, K. Y. Zhang, J. Yin, X. L. Wu and H. Zhu, *Energy Storage Mater.*, 2025, **75**, 104008.

15 H. M. Zhang, W. F. Zhang and F. Q. Huang, *ACS Appl. Mater. Interfaces*, 2021, **13**, 61180–61188.

16 S. H. Zhang, N. Sun, X. Li, R. A. Soomroa and B. Xu, *Energy Storage Mater.*, 2024, **66**, 103183.

17 Z. Tang, D. Jiang, Z. H. Fu, J. Zhou, R. Liu, R. Zhang, D. Sun, A. S. Dhmees, Y. G. Tang and H. Y. Wang, *Small Methods*, 2024, **8**, 2400509.

18 H. Au, H. Alptekin, A. C. S. Jensen, E. Olsson, C. A. O'Keefe, T. Smith, M. C. Ribadeneyra, T. F. Headen, C. P. Grey, Q. Cai, A. J. Drew and M. M. Titirici, *Energy Environ. Sci.*, 2020, **13**, 3469–3479.

19 X. R. Tian, M. Y. Sun, S. H. Luo, Q. Wang, G. Wang, L. X. Li and C. S. Li, *J. Energy Storage*, 2025, **113**, 115684.

20 X. Y. Liu, Y. Wang, Z. Y. Wang, S. Y. Zhao, N. Ju, Y. M. Wang, W. L. Zhang and H. B. Sun, *J. Energy Storage*, 2024, **101**, 113798.

21 Y. F. Chen, H. Y. Sun, X. X. He, Q. H. Chen, J. H. Zhao, Y. H. Wei, X. Q. Wu, Z. J. Zhang, Y. Jiang and S. L. Chou, *Small*, 2024, **20**, 2307132.

22 W. B. Hou, K. J. Sun, L. L. Ma, Z. Y. Liu, Y. M. Hu, W. X. Miao, B. Tao, H. Peng and G. F. Ma, *J. Energy Chem.*, 2025, **105**, 65–75.

23 Q. Z. Jin, W. Li, K. L. Wang, H. M. Li, P. Y. Feng, Z. C. Zhang, W. Wang and K. Jiang, *Adv. Funct. Mater.*, 2020, **30**, 1909907.

24 Y. F. Cao, X. H. Tang, M. N. Liu, Y. Y. Zhang, T. T. Yang, Z. P. Yang, Y. Y. Yu, Y. Li, J. T. Di and Q. W. Li, *Chem. Eng. J.*, 2022, **431**, 133241.

25 W. Wang, W. Lia, H. Lia, C. Xua, G. Zhao and Y. Ren, *J. Water Process Eng.*, 2022, **50**, 103311.

26 H. Chen, N. Sun, Y. X. Wang, R. A. Soomro and B. Xu, *Energy Storage Mater.*, 2023, **56**, 532–541.

27 M. X. Song, Q. Song, T. Zhang, X. M. Huo, Z. Z. Lin, Z. W. Hu, L. Dong, T. Jin, C. Shen and K. Y. Xie, *Nano Res.*, 2023, **16**, 9299–9309.

28 F. Xie, Z. Xu, A. C. S. Jensen, H. Au, Y. X. Lu, V. Araullo-Peters, A. J. Drew, Y. S. Hu and M. M. Titirici, *Adv. Funct. Mater.*, 2019, **29**, 1901072.

29 H. H. Lai, S. Zhang, Q. Wang, W. Zhao, Y. F. Tong, L. B. Li, C. Huang, B. K. Yap, X. W. Peng and L. X. Zhong, *Nano Energy*, 2025, **143**, 111298.

30 Y. Q. Li, Y. X. Lu, Q. S. Meng, A. C. S. Jensen, Q. Q. Zhang, Q. H. Zhang, Y. X. Tong, Y. R. Qi, L. Gu, M. M. Titirici and Y. S. Hu, *Adv. Energy Mater.*, 2019, **9**, 1902852.

31 C. C. Cai, Y. G. Chen, P. Hu, T. Zhu, X. Y. Li, Q. Yu, L. Zhou, X. Y. Yang and L. Q. Mai, *Small*, 2022, **18**, 2105303.

32 X. B. Zhao, P. Shi, H. B. Wang, Q. S. Meng, X. G. Qi, G. J. Ai, F. Xie, X. H. Rong, Y. Xiong, Y. X. Lu and Y. S. Hu, *Energy Storage Mater.*, 2024, **70**, 103543.

33 Y. L. Wang, Z. L. Yi, L. J. Xie, Y. X. Mao, W. J. Ji, Z. J. Liu, X. X. Wei, F. Y. Su and C. M. Chen, *Adv. Mater.*, 2024, **36**, 2401249.

34 Z. Tang, R. Liu, D. Jiang, S. Q. Cai, H. H. Li, D. Sun, Y. G. Tang and H. Y. Wang, *ACS Appl. Mater. Interfaces*, 2024, **16**, 47504–47512.

35 L. H. Zhang, N. Chen, S. J. Zhang, Y. H. Han, W. S. Gao and Y. X. Bai, *ACS Appl. Mater. Interfaces*, 2025, **17**, 13861–13871.

36 Y. Qian, J. W. Tian, L. B. Pan and N. Lin, *Small Methods*, 2024, **9**, 2401072.

37 S. M. Wu, Y. N. Li, L. T. Chen, Y. F. Zhang, L. X. Zeng and H. S. Fan, *Chin. Chem. Lett.*, 2025, **36**, 109796.

This journal is © The Royal Society of Chemistry 2025

J. Mater. Chem. A, 2025, **13**, 36677–36688 | **36687**

38 X. X. Liu, T. Wang, T. Y. Ji, H. Wang, H. Liu, J. Q. Li and D. L. Chao, *J. Mater. Chem. A*, 2022, **10**, 8031–8046.

39 T. Y. Zhang, T. Zhang, F. J. Wang and F. Ran, *J. Energy Chem.*, 2024, **96**, 472–482.

40 L. Li, Y. T. Li, Y. Ye, R. T. Guo, A. N. Wang, G. Q. Zou, H. S. Hou and X. B. Ji, *ACS Nano*, 2021, **15**, 6872–6885.

41 K. Y. Zhang, Y. Q. Fu, H. H. Liu, J. L. Yang, M. Y. Su, Y. L. Wang and X. L. Wu, *Phys. Scr.*, 2023, **98**, 125977.

42 Y. F. He, D. Liu, J. H. Jiao, Y. X. Liu, S. N. He, Y. Zhang, Q. Cheng, Y. G. Fang, X. L. Mo, H. G. Pan and R. B. Wu, *Adv. Funct. Mater.*, 2024, **34**, 2403144.

43 R. Chen, X. Y. Li, C. C. Cai, H. Fan, Y. J. Deng, H. G. Yu, L. Q. Mai and L. Zhou, *Small*, 2023, **19**, 2303790.

44 S. Wu, H. D. Peng, L. Huang, Y. S. Liu, Y. X. Wu, L. Liu, W. Ai and Z. P. Sun, *Inorg. Chem. Front.*, 2023, **10**, 5908–5916.

45 Z. Y. Lu, H. J. Yang, Y. Guo, H. X. Lin, P. Z. Shan, S. C. Wu, P. He, Y. Yang, Q. H. Yang and H. S. Zhou, *Nat. Commun.*, 2024, **15**, 3497.

46 W. Y. Qian, X. Y. Zhou, X. Y. Liu, M. Y. Su, K. Y. Zhang, X. L. Wu, T. Liang and X. M. Zhu, *Sci. China Mater.*, 2025, **68**(1), 309–311.

47 D. Sun, L. Zhao, P. L. Sun, K. Zhao, Y. K. Sun, Q. Zhang, Z. C. Li, Z. Ma, F. Z. Zheng, Y. Yang, C. B. Lu, C. Peng, C. M. Xu, Z. H. Xiao and X. L. Ma, *Adv. Funct. Mater.*, 2024, **34**(40), 2403642.

48 S. Wu, H. D. Peng, J. L. Xu, L. Huang, Y. S. Liu, X. C. Xu, Y. X. Wu and Z. P. Sun, *Carbon*, 2024, **218**, 118756.

49 Q. W. Meng, B. Y. Chen, W. B. Jian, X. S. Zhang, S. R. Sun, T. J. Wang and W. L. Zhang, *J. Power Sources*, 2023, **581**, 233475.

50 R. Ma, Y. X. Chen, Q. Li, B. Y. Zhang, F. F. Chen, C. Y. Leng, D. Z. Jia, N. N. Guo and L. X. Wang, *Chem. Eng. J.*, 2024, **493**, 152389.

51 H. N. He, J. He, H. B. Yu, L. Zeng, D. Luo and C. H. Zhang, *Adv. Energy Mater.*, 2023, **13**, 2300357.

52 T. Y. Xu, X. Qiu, X. Zhang and Y. Y. Xia, *Chem. Eng. J.*, 2023, **452**, 139514.

53 Y. H. Zhao, Z. Hu, C. L. Fan, P. Gao, R. S. Zhang, Z. X. Liu, J. S. Liu and J. L. Liu, *Small*, 2023, **19**, 2303296.

54 X. Y. Li, S. J. Zhang, J. J. Tang, J. Yang, K. Wen, J. Wang, P. Wang, X. Y. Zhou and Y. G. Zhang, *J. Mater. Chem. A*, 2024, **12**, 21176–21189.

55 J. H. Huang, D. Liu, Z. Y. Huang, L. Zhong, X. H. Zu, W. L. Zhang and X. Q. Qiu, *J. Power Sources*, 2024, **613**, 234863.

36688 | *J. Mater. Chem. A*, 2025, **13**, 36677–36688

This journal is © The Royal Society of Chemistry 2025